FD 171: Femtosecond x-ray diffraction maps field-driven charge dynamics in ionic crystals

Journal:	*Faraday Discussions*
Manuscript ID:	FD-ART-02-2014-000026.R1
Article Type:	Paper
Date Submitted by the Author:	11-Mar-2014

Complete List of Authors:	Woerner, Michael; Max-Born-Institute, Holtz, Marcel; Max Born Institute, C3 Juve, Vincent; Max Born Institute, C3 Elsaesser, T; Max-Born-Institute, Borgschulte, Andreas; EMPA,

CREATED USING THE RSC LaTeX PCCP ARTICLE TEMPLATE – SEE www.rsc.org/electronicfiles FOR DETAILS
PAPER www. rsc.org/faraday_d | Faraday Discussions

Femtosecond x-ray diffraction maps field-driven charge dynamics in ionic crystals

Michael Woerner,*[a] **Marcel Holtz,**[a], **Vincent Juvé,**[a] **Thomas Elsaesser,**[a] **and Andreas Borgschulte**[b]

Received Xth XXXXXXXXXX 20XX, Accepted Xth XXXXXXXXX 20XX
First published on the web Xth XXXXXXXXXX 200X
DOI: 10.1039/c000000x

X-ray diffraction provides insight into the distribution of electronic charge in crystals. Equilibrium electron distributions have been determined with high spatial resolution by recording and analysing a large number of diffraction peaks under stationary conditions. In contrast, transient electron densities during and after structure-changing processes are mainly unknown. Recently, we have introduced femtosecond x-ray powder diffraction from polycrystalline samples to determine transient electron density maps with a spatial resolution of 0.03 nm and a temporal resolution of 100 fs. In a pump-probe approach with a laser-driven tabletop hard x-ray source, optically induced structure changes are resolved in time by diffracting the hard x-ray probe pulses at different time delays from the excited powder sample and recording up to several tens of reflections simultaneously. Time-dependent changes of the atomic arrangement in the crystal lattice as well as modified electron densities are derived from the diffraction data. As a prototypical field-driven process, we address here quasi-instantaneous changes of electron density in $LiBH_4$, LiH and $NaBH_4$ in response to a non-resonant strong optical field. The light-induced charge relocation in $LiBH_4$ and $NaBH_4$ exhibits an electron transfer from the anion (BH_4^-) to the Na^+ cation. The distorted geometry of the BH_4 tetrahedron in $LiBH_4$ leads to different contributions of the H atoms to electron transfer. LiH displays a charge transfer from Li to H, i.e., an increase of the ionicity of LiH in the presence of the strong electric field. This unexpected behavior originates from strong electron correlations in LiH as is evident from a comparison with quasi-particle bandstructure calculated within the Coulomb-hole-plus-screened-exchange (COHSEX) formalism.

1 Introduction

Ultrashort optical pulses allow for applying peak electric fields to a crystal which are comparable to or even beyond the fields valence electrons experience under equilibrium conditions. In this regime of light-matter interaction, field-driven

---

[a] *Max-Born-Institut für Nichtlineare Optik und Kurzzeitspektroskopie, 12489 Berlin, Germany. Fax: +49 30 6392 1489; Tel: +49 30 6392 1470; E-mail: woerner@mbi-berlin.de*
[b] *EMPA, Swiss Federal Laboratories for Materials Testing and Research, Laboratory for Hydrogen and Energy, CH-8600 Dübendorf, Switzerland.*

processes of charge transport and nonlinear optical phenomena under non-perturbative conditions are made accessible to experiments with atto- to femtosecond time resolution. Field-driven coherent ballistic electron motions[1] and electron emission[2], interband tunneling of electrons[3], and light-driven charge relocations[4–6] are prototype phenomena. Experiments based on a variety of optical and electrooptical methods have focused on the ultrafast dynamics of electric polarizations and currents while the spatial aspects of the electronic response have remained mainly unexplored. X-ray methods with a femtosecond time resolution, in particular x-ray diffraction, provide access to spatial electron distributions during and after ultrafast processes[7–13] and, thus, hold a strong potential for unraveling field-driven processes in *space and time*.

A basic field-driven process in the ionic material $NaBH_4$ is illustrated in Fig. 1 where the ionic potentials of Na^+ and BH_4^- are shown together with the (cell-periodic) electron wavefunctions in the highest valence band (vb) and the lowest conduction band (cb) state. Under equilibrium conditions, the vb wavefunction $|\Psi_{vb}\rangle$ shows a high amplitude on the BH_4^- and a small amplitude on the Na^+ ion. A strong external field of an amplitude comparable to the interionic field of approximately 10^9 V/m distorts the ionic potentials and leads to the admixture of other ionic states, in particular conduction band states $|\Psi_{cb}\rangle$ with a similar amplitude on the two sites. The new wavefunction is given by $|\Psi_{virt}\rangle = \alpha|\Psi_{cb}\rangle + \beta|\Psi_{vb}\rangle$[14], describing a state in which. electronic charge is shifted from the BH_4^- to the Na^+ ion over the inter-ionic distance of some 300 pm. This mechanism generates a strong electric polarization of the material existing as long as the external field is present.

The elementary picture outlined in Fig. 1 neglects modifications of the charge distribution originating from the inherent long-range electron-electron interactions and their screening in the densely packed crystal lattice. Consequently, it remains open to what extent the picture of Fig. 1 exists and which modifications are introduced by the coulomb correlations among electrons. While such issues have been addressed for model systems in the theoretical literature[15–26], experimental insight into field-driven electron relocations is scarce. Ultrafast time-resolved x-ray diffraction allows for testing the validity of the picture of Fig. 1 and - vice versa - should allow for probing the impact of correlations effects on transient electron distributions.

In this article, we demonstrate and discuss the potential of femtosecond x-ray powder diffraction[27] to measure transient electron density maps induced by a strong external optical field under nonresonant conditions. Our work is focused on the ionic materials LiH and $NaBH_4$, consisting of light elements and, thus, allowing for a mapping of valence electrons. While $NaBH_4$ displays a behavior expected for an ionic crystal, i.e., a shift of electronic charge from the negative BH_4^- ion to the positive Li^+ ion, LiH behaves differently. Here, charge is shifted from Li to H, enhancing the ionicity of the material. We show that this unexpected behavior is a direct consequence of electron-electron corelations reproduced by theoretical bandstructure calculations within the Coulomb-hole-plus-screened-exchange (COHSEX) formalism.

The article is organized as follows. Section 2 gives a brief summary of the experimental method and data. The analysis of the diffraction data and extraction of electron density maps are discussed in detail in section 3, followed by a dis-

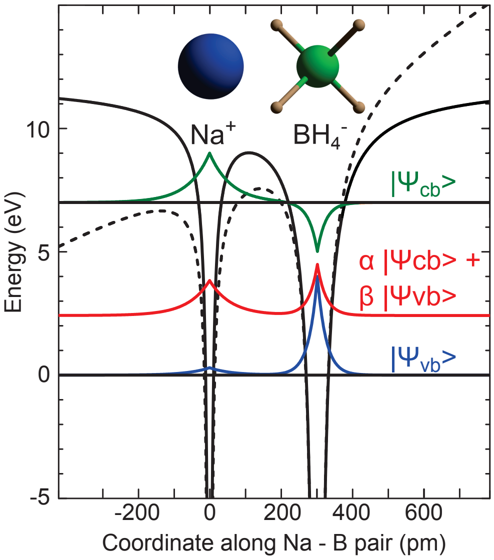

Fig. 1 Schematic illustrating the mechanism of electron transfer from a BH_4^- to a Na^+ ion in a $NaBH_4$ crystal. The unperturbed valence and conduction band wavefunctions, Ψ_{vb} and Ψ_{cb} (blue and green curves), and the ionic potentials (solid black lines) are plotted as a function of the inter-ionic distance. In the valence band, electrons are mainly localized on the BH_4^- ion while the conduction band wavefunction displays similar amplitudes on the two ions. Upon application of an external electric field with an amplitude comparable to the inter-ionic fields, the potentials are distorted (dashed black line) and the corresponding perturbed wavefunction $\alpha\Psi_{vb} + \beta\Psi_{cb}$ (red line) is a mixture of valence and conduction band states of the unperturbed Hamiltonian. Generation of this virtual state is connected with a partial electron transfer from the BH_4^- to the Na^+ ion and a strong electric polarization. In time, the electron transfer follows the external electric field.

cussion of the results for $NaBH_4$ and LiH in section 4. Bandstructure theory and its application to the electron density maps are presented in section 5, followed by conclusions in section 6.

2 Femtosecond x-ray diffraction experiment

In a femtosecond pump-probe scheme, the electric field of a nonresonant 800 nm excitation pulse interacts with a powder sample and a synchronized hard x-ray probe pulse is diffracted from the sample at different fixed time delays. The angular positions and intensities of several Debye Scherrer rings which are of elliptic or hyperbolic shape on the two-dimensional x-ray detector, are recorded simultaneously and represent the primary data from which transient electron density maps are derived. Pump and probe pulses are derived from an amplified Ti:sapphire laser system delivering sub-50 fs pulses centered at 800 nm with an energy per pulse of 5 mJ and a repetition rate of 1 kHz. The excitation pulses have a peak amplitude of the electric field of approximately 1 GV/m. The main

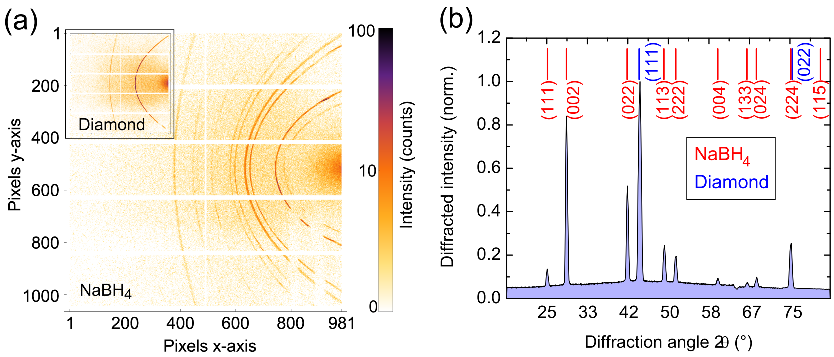

Fig. 2 (a) X-ray diffraction pattern of the $NaBH_4$ powder sample as recorded with a large-area x-ray detector. The inset shows the diffraction pattern of the diamond windows only. (b) Diffracted x-ray intensity integrated over individual Debye-Scherrer rings from $NaBH_4$ as a function of the diffraction angle 2θ.

fraction of the laser output drives a plasma source[28] providing hard x-ray pulses of a photon energy of 8.06 keV (Cu Kα) and a duration of approximately 100 fs. The x-ray diffraction patterns are detected with a large area detector (Pilatus Dectris 1M). Each diffraction ring corresponds to one (or several equivalent) set(s) of lattice planes *hkl* [Fig. 2(a)]. The exposure time per time delay step was 140 s and typically ≈ 2000 time delay steps were collected for several days with a fresh sample everyday. The all optical autocorrelation was measured repeatedly to assure a proper stacking of the different data sets.

The $NaBH_4$ and LiH samples consist of a 200 μm thick powder, pressed inbetween and sealed by two 20 μm thick diamond windows. Assuming a spherical shape of ions in the crystal lattice, both $NaBH_4$ and LiH crystallize in a rock-salt structure (space group $Fm\bar{3}m$) with lattice constants of $a = 407.52$ pm (LiH)[29,30] and $a = 615.06$ pm ($NaBH_4$)[31,32]. At T=300 K, $LiBH_4$ crystallizes in the orthorhombic space group Pnma (No. 62). The unit cell dimensions are a=0.718 nm, b=0.444 nm, c=0.680 nm[33] with four formula units per unit cell. Because of the high chemical reactivity, great care was taken to avoid air contamination of the sample which was prepared under an Ar atmosphere in a glove-box. During the measurements, the samples were continuously rotated.

In Fig. 2, we present diffraction patterns of $NaBH_4$ while similar data for LiH and $LiBH_4$ have been reported in Refs.[13] and[12], respectively. Fig. 2(a) displays part of the detected ring pattern whereas Fig. 2(b) shows the intensity integrated over the stationary diffraction rings of $NaBH_4$ as a function of the diffraction angle 2θ. Two diamond reflections (blue) originate from the sample windows. When applying the field of the excitation pulse, we observe changes of diffracted intensity of the diffraction rings in all three samples with the angular positions remaining unchanged. In Fig. 3(a) and (b) the change of diffracted intensity on the (111) rings in $NaBH_4$ and LiH is plotted as a function of pump-probe delay. In panels (c-f) we show transient intensity changes for 4 selected allowed reflections of $LiBH_4$ as a function of pump-probe delay (symbols). Depending on the investigated material and the diffraction ring (*hkl*), one observes either

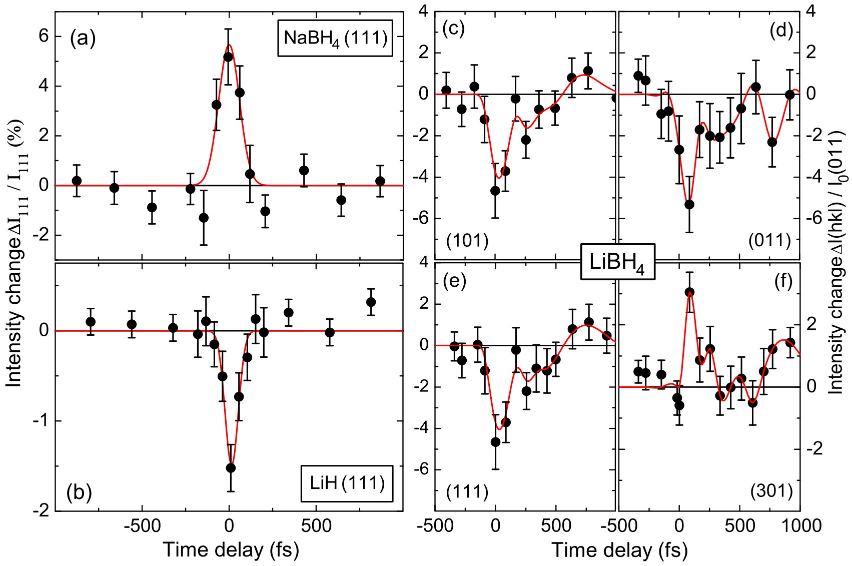

Fig. 3 (a) Relative change of diffracted intensity of $NaBH_4$ by the (111) plane versus the pump-probe time delay. (b) Relative change of the diffracted intensity of LiH by the (111) plane versus time delay. (c-f)Transient intensity changes for 4 selected allowed reflections measured on $LiBH_4$ powder as a function of pump-probe delay (symbols). The red lines are gaussian fits in panels (a) and (b) and B-splines in (c-f) as guides to the eye.

an increase [(a) and (f)] or a decrease [panels ((b)-(e)] of diffracted intensity of a few percent around delay zero when excitation and probe pulses interact simultaneously with the sample. For $NaBH_4$ and LiH the temporal behavior follows essentially the cross correlation between excitation and probe pulses. In $LiBH_4$ we observe some small longer-lived intensity changes. This fact shows that the induced changes exist mainly with the excitation field present and that they are fully reversible.

The relative intensity change of the diffraction ring *hkl* is given by

$$\frac{\Delta I_{hkl}(t)}{I_{hkl}} = \frac{|F_{hkl}(t)|^2 - |F^0_{hkl}|^2}{|F^0_{hkl}|^2}, \qquad (1)$$

where $F_{hkl}(t)$ is the structure factor of the material modified by the external electric field and F^0_{hkl} the known structure factor of the unexcited crystal. The structure factors are related to the electronic density $\rho(\mathbf{r})$ by a Fourier transform. The steady-state electronic density $\rho_0(\mathbf{r})$ is given by the Fourier transform of the structure factors F^0_{hkl}. At room temperature in all three materials $NaBH_4$, LiH, and $LiBH_4$ the structure factors are real due to the inversion symmetry of the rock-salt structure (space group $Fm\bar{3}m$) or the orthorhombic space group *Pnma*.

---

3 Reconstruction of the transient electron density $\rho(\mathbf{r},t)$

The equilibrium charge density $\rho_0(\mathbf{r})$ can be derived from the known structure and structure factors of the unexcited crystals[29–33]. To determine the transient $\rho(\mathbf{r},t)$ from the measured transient diffraction patterns, the phase factors of the structure factors $F_{hkl}(t)$ need to be known. The principal strategy for solving this problem is discussed next.

When measuring a fully disordered powder sample, the electric field vector of the excitation pulse $\mathbf{E}(t)$ has an individual orientation relative to the crystal axes in each crystallite. The transient change of the electron density in a particular crystallite *i*, $\Delta\rho_i(\mathbf{r},t) = \rho_i(\mathbf{r},t) - \rho_0(\mathbf{r})$ can be decomposed into symmetry conserving and a non-conserving component $\Delta\rho_i(\mathbf{r},t) = \Delta\rho^{\mathrm{Sym}}(\mathbf{r},|\mathbf{E}(t)|) + \Delta\rho_i^{\mathrm{NoSym}}(\mathbf{r},\mathbf{E}(t))$. The symmetry conserving part depends only on the amplitude of the electric field $|\mathbf{E}(t)|$ and, thus, is identical in all crystallites. Since the distribution of relative orientations between $\mathbf{E}(t)$ and the crystal axes is isotropic in a powder sample, the symmetry conserving electron density change is just the electron density change averaged over all crystallites: $\Delta\rho_{\mathrm{Sym}}(\mathbf{r},t) = N^{-1}\sum_{i=1}^{N}\Delta\rho_i(\mathbf{r},t)$. In this averaging procedure, the symmetry non-conserving components cancel each other since for each crystallite *a* with $\Delta\rho_a^{\mathrm{NoSym}}(\mathbf{r},\mathbf{E}(t))$ the ensemble contains another crystallite *b* with $\Delta\rho_b^{\mathrm{NoSym}}(\mathbf{r},\mathbf{E}(t)) = -\Delta\rho_a^{\mathrm{NoSym}}(\mathbf{r},\mathbf{E}(t))$. As a consequence, $\Delta\rho_{\mathrm{Sym}}(\mathbf{r},t)$ exhibits the symmetry properties of the initial structure $\rho_0(\mathbf{r})$. Please note that $\Delta\rho_{\mathrm{Sym}}(\mathbf{r},t)$ is exclusively determined by the intensity changes of the *allowed* reflections. In the case of $LiBH_4$ we observed also a small amount of transient intensity on forbidden reflections (see our discussion of this phenomenon in Ref.[12]). In the more recent studies on LiH and $NaBH_4$ any detectable intensity on forbidden reflections was absent and, thus, the symmetry non-conserving component is negligible compared to $\Delta\rho_{\mathrm{Sym}}(\mathbf{r},t)$. The following discussion focuses exclusively on $\Delta\rho_{\mathrm{Sym}}(\mathbf{r},t)$.

3.1 Maximum entropy method (MEM)

The MEM aims at finding the most likely charge-density distribution by maximizing the quantity $S = -\sum_{i=1}^{N_{pix}} \rho_i \log(\rho_i)$ (formally similar to the entropy, hence the name) under the constraints given by the information obtained from the experiment[34,35]. The quantities ρ_i are the electron density at a position i in space, the so-called pixel i. The total number of pixels is N_{pix}. The MEM effectively exploits all the information from the experiment without creating artifacts in the charge density distribution. The quantity *S* cannot be maximized analytically but is calculated recursively, e.g., by the Sakata-Sato algorithm[36] implemented in the BayMEM program[37].

In general, an exact Fourier transform for determining the spatially resolved electron density requires an infinite number of structure factors F_{hkl}. In practice, any diffraction experiment only gives the structure factors for a limited number of reflections, typically restricted by an upper limit for the diffraction angle $2\Theta_{\max}$. In such an incomplete data set, the scattering vector $q_{\max} = \sin(\Theta_{\max})/\lambda$ determines the spatial resolution at which the electron density map $\rho(\mathbf{r},t)$ can be reconstructed. For an unbiased analysis of the transient electron density $\rho(\mathbf{r},t)$,

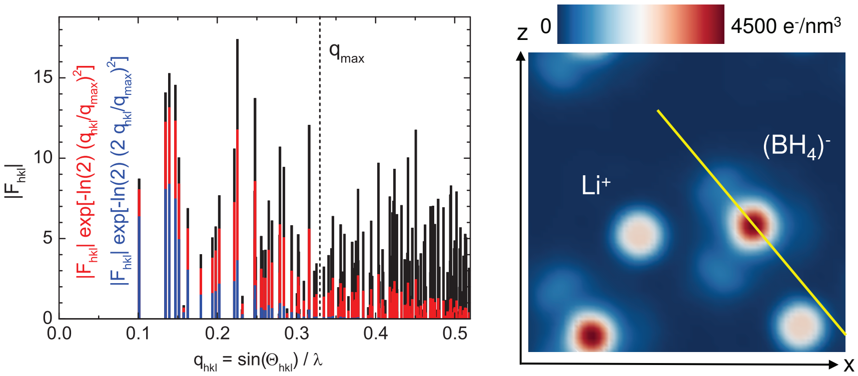

Fig. 4 (a) Amplitudes of structure factors of $\mathrm{LiBH_4}$ as a function of $q = \sin(\Theta)/\lambda$ for different spatial resolutions. $q_{\max} = \sin(\Theta_{\max})/\lambda$ indicates the reflections measured in our femtosecond diffraction experiment. (b) Stationary total electron density distribution in the plane Y=0.25), convoluted in the reciprocal space with a gaussian [red columns in panel (a)] to fit our spatial resolution. The yellow line indicates the section along Fig. 7(a) is plotted.

we prefer to avoid any refinement of the data, e.g., with least-squares methods starting from a model of the transient structure.

The MEM allows for a reconstruction of $\rho(\mathbf{r},t)$ from the experimentally observed reflections (F_{hkl}^{obs}) with $|q_{hkl}| < q_{\max}$ without involving any model. A brief introduction to the MEM can be found in chapter 5.3 of Ref.[38]. There has been quite some controversy about the application of the MEM, mainly caused by claims of a spatial 'super-resolution'[39] or the 'proof' of non-nuclear maxima of $\rho(\mathbf{r})$ in silicon[36]. In a proper application of the MEM, the amount of added unknown information, i.e., the structure factors F_{hkl}^{MEM} with $|q_{hkl}| > q_{\max}$, has to be definitely smaller than the experimentally known information F_{hkl}^{obs}. In contrast to least-squares methods the concept of the MEM allows for making the differences $|F_{hkl}^{\mathrm{MEM}} - F_{hkl}^{\mathrm{obs}}| \ll |F_{hkl}^{\mathrm{obs}}|$ arbitrarily small.

Our previous reconstruction of $\rho(\mathbf{r},t)$ of $\mathrm{LiBH_4}$ has been based on a published analysis of the equilibrium structure which has been determined with the least-squares method within the independent atom model[33]. The amplitude of the structure factors F_{hkl} are shown as black bars in Fig. 4. The corresponding charge density was used as the initial guess, the so-called PRIOR in the MEM[37]. Structure factors of overlapping Debye Scherrer rings were treated within the MEM using the so called "group amplitudes"[40].

Applying the MEM directly to the experimentally observed reflections (F_{hkl}^{obs}) with $|q_{hkl}| < q_{\max}$ leads to unreliable predictions since the amount of forecast information (i.e. F_{hkl}^{MEM} with $|q_{hkl}| > q_{\max}$) is larger than that from the experiment covering the range of $|q_{hkl}| < q_{\max}$. To circumvent this problem, we artificially reduced the spatial resolution in deriving both $\rho_0(\mathbf{r})$ and $\rho(\mathbf{r},t)$ by multiplying the corresponding structure factors with a gaussian profile $F_{hkl} \times \exp[-\ln(2)(q_{hkl}/q_{\max})^2]$. The resulting structure factors are shown as red bars in Fig. 4(a).

The corresponding electron stationary electron density $\rho_0(x, 0.25b, z)$ in the

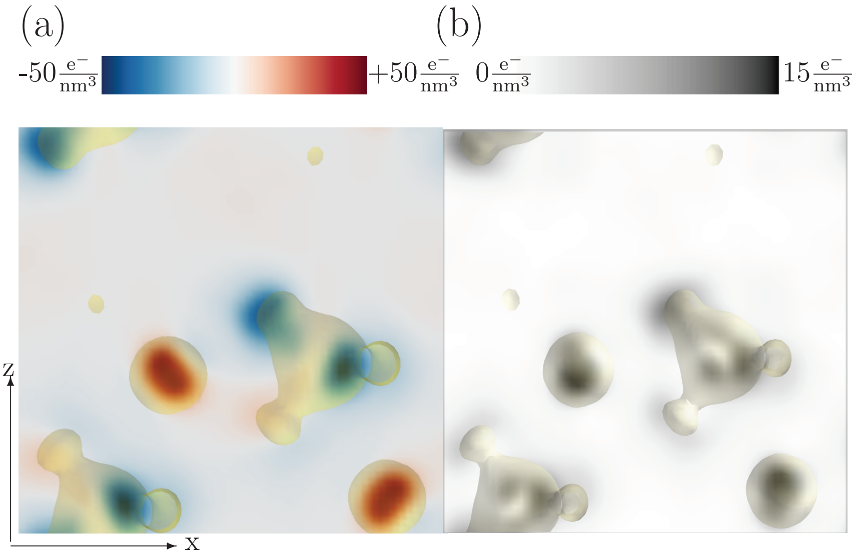

Fig. 5 Comparison between (a) the transient electron density map $\Delta\rho_{\mathrm{Sym}}$ of $LiBH_4$ at $\tau = 0$ [Fig. 3(c) of Ref.[12]] together with (b) the spatially resolved error of such a map obtained from the fluctuations of maps measured at negative delay times $\tau < 0$.

plane where the Li-, the B-, and two H-atoms of a $LiBH_4$ molecule reside is shown in Fig. 4(b). This spatial resolution corresponds to the experimental one and, thus, the MEM is not enhancing the spatial resolution, but just helps to avoid artifacts because of the abrupt end of the Fourier series, e.g., the so-called Gibbs phenomenon (the appearance of ring-like structures around the atoms) in the charge-density distribution. Due to the low Z of all atoms in $LiBH_4$ one can clearly see the hydrogen atoms in the vicinity of the boron atom [Fig. 4(b)]. However, reducing the spatial resolution further, $F_{hkl} \times \exp[-\ln(2)(2q_{hkl}/q_{\max})^2]$ [blue bars in Fig. 4(a)] leads to the situation that the MEM result shows an almost vanishing difference from the direct Fourier transform in the truncated reciprocal space, i.e. $F_{hkl} = 0$ for $|q_{hkl}| > q_{\max}$.

To summarize, the MEM allows for a gradual transition from an exact reconstruction towards being increasingly speculative when increasing the (gaussian) spatial resolution from $q_{\mathrm{gauss}} < q_{\max}$ to $q_{\mathrm{gauss}} > q_{\max}$. Such an analysis avoids artefacts and allows for a proper assessment of the MEM results. This method has been applied for extracting the transient electron density maps of $NaBH_4$, LiH, and $LiBH_4$ from our femtosecond powder diffraction data.

3.2 Signal-to-noise-ratio of transient electron density maps

The signal-to-noise ratio of a transient electron density map is estimated by the procedure described in the following. Maps measured at negative delay times $\tau < 0$ show fluctuations with an amplitude strongly depending on the value of the electron density at a particular spatial position within the unit cell. The standard deviation of such fluctuations gives the amplitude of an error bar shown in Fig. 5(b) which is 3-4 times smaller than the largest transient changes $\Delta\rho(\mathbf{r},t)$

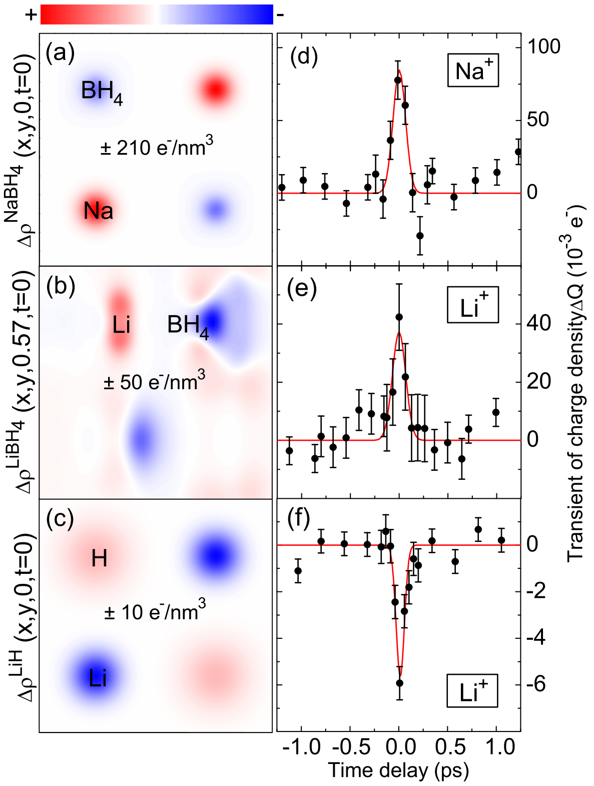

Fig. 6 (a) Difference electronic density map $\Delta\rho(\mathbf{r},t=0)$ reconstructed by the MEM at zero delay time of $NaBH_4$. (b) and (c) $\Delta\rho(\mathbf{r},t=0)$ of $LiBH_4$ and LiH, respectively. In contrast to the boron hydrides (i.e. charge transfer from anion to cation) LiH shows an increase of its ionicity when exposed to the strong electric field of the pump pulse. (d-f) Integrated charge changes on the respective cation Na or Li versus the delay time.

shown in Fig. 5(a). Typically, such fluctuations are large at spatial positions of high electron density, e.g., on the boron atoms in Fig. 5(b). However, the position of an atom within the unit cell plays also a significant role for the size of the error bar. In particular, one gets a very high signal-to-noise ratio for $\Delta\rho(\mathbf{r},t)$ in situations if electronic charge transiently appear at spatial positions where initially no atom was present, e.g. hydrogen atoms in $(NH_4)_2SO_4$[9].

4 Discussion and analysis of the transient charge density maps

Using the MEM described in the previous section we reconstructed from our femtoseond x-ray diffraction data (Fig. 3) the corresponding transient charge density maps $\Delta\rho(\mathbf{r},t=0)$ which are shown for time delay zero in Fig. 6. In panel (a) we show the difference electron density map of $NaBH_4$. The difference maps $\Delta\rho(\mathbf{r},t=0)$ of $LiBH_4$ and LiH are presented in panels (b) and (c). Another sectional view of $\Delta\rho(\mathbf{r},t=0)$ of $LiBH_4$ has already been shown in Fig. 5(a). We now discuss the exchange of electronic charge between cations and anions, as well as details of transient charge changes on the hydrogen atoms which are clearly detected with our spatial resolution for $LiBH_4$.

4.1 Transient exchange of electronic charge between cations and anions

The initial electron density map $\rho_0(x, y, 0)$ of LiH with our spatial resolution is shown in Fig. 2(a) of Ref.[13] and exhibits a high electron density on the Li atom and a small density on the H atom. In Fig. 6(c), the change of electron density $\Delta\rho_{sym}(\mathbf{r}, t)$ is plotted for zero delay time. This map shows a pronounced decrease of electron density on the Li atom and a corresponding increase on the hydrogen position, giving direct evidence for a quasi-instantaneous increase of the ionicity of LiH in the presence of the strong electric field. This surprising behavior is in strong contrast to $\Delta\rho_{sym}(\mathbf{r}, t)$ of $NaBH_4$ [Fig. 6(a)] and $LiBH_4$ [Fig. 6(b)], where the light-induced charge relocation exhibits an expected charge transfer from the anion (BH_4^-) to the respective cation.

To determine the amount of charge transferred, we divided the unit cell into sub-volumes, i.e., each spatial position $\mathbf{r}$ within the unit cell is uniquely assigned to the sub-volume of the nearest atom. We then integrated the charge in the sub-volumes. For LiH this procedure leads to $(a/2)^3$ cubes around Li and H. In the case of BH_4^- anions, the charge of the whole unit was put together. Time-dependent charge density changes are displayed in Fig. 6(d) to (f) where we plotted the integrated charge changes on the respective cation, i.e. Na^+ or Li^+, versus the delay time.

In LiH, the striking feature is a sharp drop of electronic charge on the Li atom [Fig. 6(f)] concomitant with the increase of the same amplitude on the hydrogen position due to charge conservation within each unit cell. The peaks of the transients in panels (d-f) have a width of ≈ 100 fs (FWHM) which agrees with the temporal cross-correlation function of the optical excitation and the hard x-ray probe pulses[9,12]. In the case of the boron hydrides [Fig. 6(d) and (e)] we see exactly the opposite behavior, i.e., a light-induced charge transfer from the anion BH_4^- to the respective cation Na^+ or Li^+. Outside the temporal overlap of pump and probe pulses, the changes of electron density are minor. Such facts strongly support our picture of a field-driven charge transfer which is limited in time to the presence of the driving field.

In summary, LiH shows an increase of its ionicity when exposed to the strong electric field of the pump pulse, in contrast to the boron hydrides where the charge transfer from the anion to the cation reduces the ionicity.

4.2 Asymmetric transient charge changes on the H-atoms within the distorted BH_4 tetrahedron of $LiBH_4$

In the case of $LiBH_4$ our spatial resolution allows for analyzing details of transient charge changes on the hydrogen atoms. In particular we can identify an asymmetric transient charge change on one of the H-atoms within the distorted BH_4 tetrahedron of $LiBH_4$. To this end we plot in Fig. 7(a) the stationary electronic density $\rho_0(\mathbf{r}_{B-H})$ of $LiBH_4$ (blue curve) along the connecting line $\mathbf{r}_{B-H}$ between the boron atom and one hydrogen atom within the BH_4^- anion. This path indicated by the yellow line in Fig 4(b) traverses in part the electron cloud of a

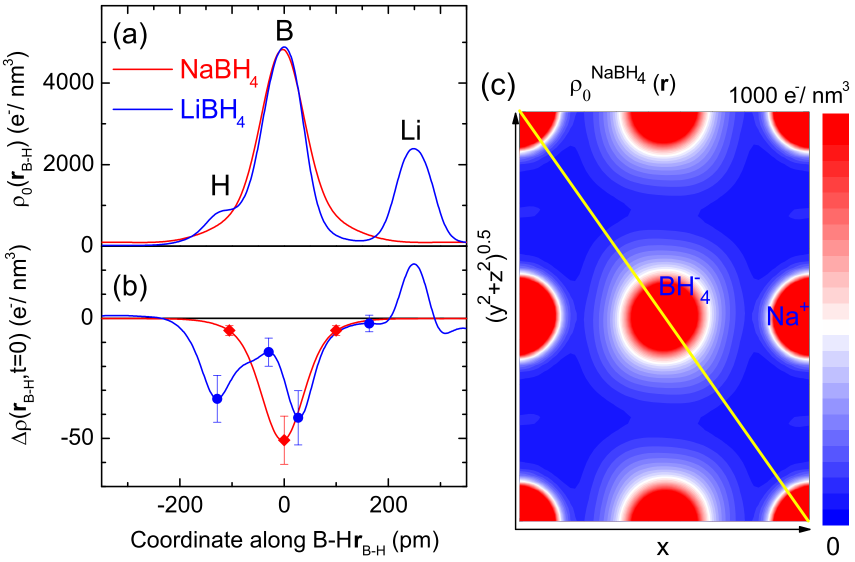

Fig. 7 (a) Stationary electronic density $\rho_0(\mathbf{r}_{\mathrm{B-H}})$ along the connecting line between the boron atom and one hydrogen atom [yellow lines in panel (c) and in Fig 4(b)] within the BH_4^- anion for $LiBH_4$ (blue curve) and $NaBH_4$ (red curve). (b) Respective electron density change $\Delta\rho(\mathbf{r}_{\mathrm{B-H}}, t=0)$ along the connecting lines. The error bars are calculated by means of the method described in section 3.2.

Li-atom but not those of the other 3 H-atoms. For comparison we plot a similar curve for $NaBH_4$ (red line). Although our spatial resolution was somewhat higher in the $NaBH_4$ experiment (i.e. larger $q_{\max}$) we can clearly distinguish the hydrogen atoms from their boron atom for the BH_4^- ion in $LiBH_4$. The invisibility of hydrogens in $NaBH_4$ is due to the statistical mixture of hydrogen atoms belonging with 50% probability to two different tetrahedrons having their corners on a cube around the boron atom (Wyckoff positions 32 f of space group $Fm\bar{3}m$). In Fig. 7(b) we show the electron density changes $\Delta\rho(\mathbf{r}_{\mathrm{B-H}}, t=0)$ for the two materials along the respective connecting lines. In the case of $NaBH_4$ the entire anion loses its charge without displaying an internal structure of $\Delta\rho(\mathbf{r}_{\mathrm{B-H}}, t=0)$ within the BH_4^- ion. In contrast, we observe a pronounced asymmetric transient charge change within the BH_4 tetrahedron of $LiBH_4$ [blue curve in Fig. 7(b) and difference charge density map in Fig. 5(a)]. Electronic charge is lost on one of the H-atoms (left minimum) and the antipodal orbital of the B-atom (right minimum). In $LiBH_4$ the structure of the tetrahedrons is distorted with different lengths and angles of the B-H bonds[33]. Interestingly, the hydrogen H1 with the shortest bond length [$d_{\mathrm{B-H1}} = 104$ pm, cf. Table 2 of Ref.[33]] dominates in the charge loss of the anion. We consider this distortion the origin of the inequivalent charge transfer from the different hydrogens.

4.3 Microscopic mechanism of field-induced charge transfer between ions

We now discuss the microscopic physics underlying the material's polarization and the field-induced change of electron density $\Delta\rho_{sym}(\mathbf{r}, t)$ in the different materials. Without external field, electrons in an insulator populate states up to the highest valence band. An external field of an amplitude comparable to the interionic field of the order of 1 GV/m distorts the ionic potentials and leads to the admixture of other ionic states, in particular conduction band states (cf. Fig. 1). The wavefunction of the mixed state is given by

$$|\Psi_{b,\mathbf{k}}(\mathbf{E})\rangle = \frac{1}{\sqrt{N}}\left[|\Psi_{b,\mathbf{k}}\rangle + \mathbf{E}\sum_{b'\neq b}\frac{\langle\Psi_{b',\mathbf{k}}|e\mathbf{r}|\Psi_{b,\mathbf{k}}\rangle}{\varepsilon_{b,\mathbf{k}}-\varepsilon_{b',\mathbf{k}}}|\Psi_{b',\mathbf{k}}\rangle\right] \tag{2}$$

at wave vector $\mathbf{k}$ in the (occupied) band b with the normalization constant N. The sum runs over all unoccupied bands b'. The perturbative approach in (2) is valid as the dipole interaction energy $|\langle\Psi_{b',\mathbf{k}}|e\mathbf{r}|\Psi_{b,\mathbf{k}}\rangle|\cdot|\mathbf{E}| \simeq 0.2$ eV is much smaller than the smallest bandgap $\varepsilon_{b,\mathbf{k}}-\varepsilon_{b',\mathbf{k}} \simeq 5$ eV of the three materials, i.e. LiH at the X point of the Brillouin zone. In other words, the experiments are in the regime of a linear response of the material to the external electric field. The symmetry conserving part of the deformed charge density is obtained by averaging over all electric field directions ($\hat{\mathbf{e}}_\Omega$: unit vector in solid angle direction Ω) and a summation over all occupied states within the Brillouin zone

$$\rho_{\mathrm{Sym}}(\mathbf{r},t) = \sum_{b,\mathbf{k}}^{\text{occupied}} \frac{1}{4\pi}\int d\Omega\, \left|\Psi_{b,\mathbf{k}}(\hat{\mathbf{e}}_\Omega\cdot|\mathbf{E}(t)|,\mathbf{r})\right|^2. \tag{3}$$

The distorted wave function (2) shows that both the eigen-energies $\varepsilon_{b,\mathbf{k}}$ (i.e., the band structure) and the eigen-functions $\Psi_{b,\mathbf{k}}(\mathbf{r})$ (i.e., the Bloch functions) of the system Hamiltonian determine the exact shape of the electron density (3) in the strong electric field.

5 Theory

The experimental results were analyzed by the model calculations presented in this section. We show that a mean-field theory such as the Hartree-Fock approximation fails to account for the experimentally observed quasi-instantaneous increase of the ionicity of LiH in the presence of the strong electric field. However, calculations including Coulomb correlations on the most basic level, i.e., quasi-particle bandstructures calculated within the Coulomb-hole-plus-screened-exchange (COHSEX) formalism[20,23], predict the increase of the ionicity of LiH correctly. In the following, we use the mathematical nomenclature introduced in Refs.[23] and[22].

The COHSEX formalism considers the dynamics of the one-particle Green's function, expands the self-energy operator in terms of a dynamically screened interaction (rather than a bare Coulomb interaction), and keeps the first term in such an expansion. The quasiparticle excitations in a closed shell many-electron system obey the integro-differential equation

$$\left[\frac{\mathbf{p}^2}{2m} + V_N(\mathbf{r}) + V_H(\mathbf{r})\right]\psi_{n,\mathbf{k}}(\mathbf{r}) + \int d\mathbf{r}'\,\Sigma(\mathbf{r},\mathbf{r}',E_{n,\mathbf{k}})\psi_{n,\mathbf{k}}(\mathbf{r}') = E_{n,\mathbf{k}}\psi_{n,\mathbf{k}}(\mathbf{r}) \tag{4}$$

where $V_N(\mathbf{r})$ is the nuclear Coulomb potential, $V_H(\mathbf{r})$ is the average Coulomb (Hartree) potential due to the electrons, and Σ is the electron self energy operator

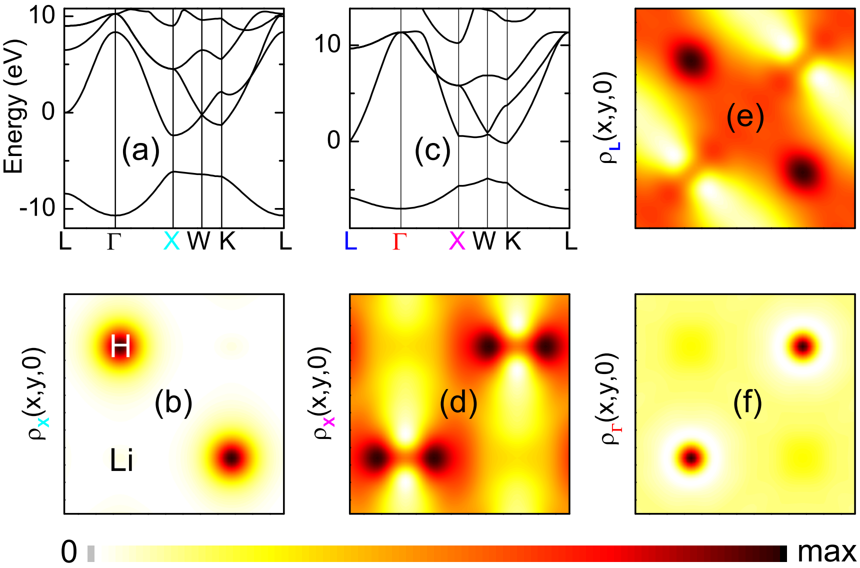

Fig. 8 (a) and (c) Quasi-particle band structures of LiH within the COHSEX approximation. (b) and (d) Stationary electron densities at the X-point, (e) L-point, and (f) Γ-point within the Brillouin zone (BZ). Panels (a) and (b) correspond to a calculation with homogeneous screening similar to that of Ref.[22] leading to a 1S-like orbital on the H atom throughout the BZ. Panels (c,d,e,f) are calculated with a somewhat stronger screening on the proton resulting in 2P-like orbitals on both Li and H nuclei at the X-point (zone boundary).

which includes all the exchange and correlation effects. It is in general a non-local, energy-dependent, non-Hermitian operator. The procedure for finding the quasi-particle energies $E_{n,\mathbf{k}}$ and wave functions $\psi_{n,\mathbf{k}}(\mathbf{r})$ requires evaluating Σ and then solving Eq. (4). In the following we use the static COHSEX approximation (first introduced by Hedin[20]) which constitutes one of the biggest steps in the theoretical basis for band structure calculations. In this approximation, the self energy is purely real (i.e. no finite quasi-particle lifetimes) and does not depend on the quasi-particle energy itself. As a consequence Eq. (4) mathematically resembles a nonlinear "Schrödinger equation" with all its advantages for solving it. For our purpose it is convenient to expand the quasi-particle wave function in plane waves [Eq. (B2) of Ref.[23]]

$$\psi_{n,\mathbf{k}}(\mathbf{r}) = \frac{1}{\sqrt{\Omega}} \sum_{\mathbf{G}} \psi_{n,\mathbf{k}}(\mathbf{G}) e^{i(\mathbf{k}+\mathbf{G})\mathbf{r}} \tag{5}$$

where $\mathbf{G}$ are the reciprocal lattice vectors of the crystal and $\Omega = N\,\Omega_{\mathrm{uc}}$ stands for the crystal volume determining the discretization in k space. $\Omega_{\mathrm{uc}} = a^3/4$ is the volume of the primitive unit cell. The quasi-particle equation now has the form

$$\sum_{\mathbf{G}'} \left[H^0_{\mathbf{G},\mathbf{G}'}(\mathbf{k}) + \Omega\, \Sigma_{\mathbf{G},\mathbf{G}'}(\mathbf{k}) \right] \psi_{n,\mathbf{k}}(\mathbf{G}') = E_{n,\mathbf{k}} \psi_{n,\mathbf{k}}(\mathbf{G}). \tag{6}$$

Both $H^0_{\mathbf{G},\mathbf{G}'}(\mathbf{k})$ and $\Sigma_{\mathbf{G},\mathbf{G}'}(\mathbf{k})$ contain purely local (i.e. k-independent) and nonlocal (i.e. k-dependent) contributions:

$$\begin{aligned}
H^0_{\mathbf{G},\mathbf{G}'}(\mathbf{k}) &= \frac{\hbar^2|\mathbf{k}+\mathbf{G}|^2}{2m}\delta_{\mathbf{G},\mathbf{G}'} + \frac{4\pi\, e^2}{\Omega_{\mathrm{uc}}|\mathbf{G}-\mathbf{G}'|^2}\left[\rho_e(\mathbf{G}-\mathbf{G}')-\rho_N(\mathbf{G}-\mathbf{G}')\right] &(7)\\
\rho_e(\mathbf{G}) &= \frac{2}{N}\sum_{n,\mathbf{k},\mathbf{G}''}^{\mathrm{occ}} \psi^*_{n,\mathbf{k}}(\mathbf{G}'')\psi_{n,\mathbf{k}}(\mathbf{G}''+\mathbf{G}), &(8)\\
\rho_N(\mathbf{G}) &= Z_{\mathrm{Li}}\, e^{i\,\mathbf{G}\,\mathbf{R}_{\mathrm{Li}}} + Z_{\mathrm{H}}\, e^{i\,\mathbf{G}\,\mathbf{R}_{\mathrm{H}}}, &(9)
\end{aligned}$$

The Fourier transform of the electron density $\rho_e(\mathbf{G})$ in Eq. (8) is identical to the structure factor $F_{hkl}=\rho_e(\mathbf{G}_{hkl})$ determined in an x-ray diffraction experiment. In the sum over occupied states with band index n and wave vector $\mathbf{k}$ (within the 1^{st} BZ), only the states of the same spin as $(n,\mathbf{k})$ contribute and the factor 2 accounts for the spin degeneracy. The self energy $\Sigma_{\mathbf{G},\mathbf{G}'}(\mathbf{k})$ consists of a nonlocal screened exchange (SEX) and a purely local Coulomb hole (COH) contribution:

$$\begin{aligned}
\Sigma^{\mathrm{SEX}}_{\mathbf{G},\mathbf{G}'}(\mathbf{k}) &= -\frac{1}{\Omega}\sum_{n,\mathbf{k}'}^{\mathrm{occ}}\sum_{\mathbf{G}_1,\mathbf{G}_2}\psi_{n,\mathbf{k}'}(\mathbf{G}-\mathbf{G}_1)\psi^*_{n,\mathbf{k}'}(\mathbf{G}'-\mathbf{G}_2)\\
&\quad\times\ \varepsilon^{-1}_{\mathbf{G}_1,\mathbf{G}_2}(|\mathbf{k}-\mathbf{k}'|,\omega=0)\,\frac{4\pi\, e^2}{\Omega|\mathbf{k}-\mathbf{k}'+\mathbf{G}_2|^2}, &(10)\\
\Sigma^{\mathrm{COH}}_{\mathbf{G},\mathbf{G}'} &= \frac{1}{\Omega}\sum_{n,\mathbf{q}}\sum_{\mathbf{G}_1,\mathbf{G}_2}\psi_{n,\mathbf{k}-\mathbf{q}}(\mathbf{G}-\mathbf{G}_1)\psi^*_{n,\mathbf{k}-\mathbf{q}}(\mathbf{G}'-\mathbf{G}_2)\\
&\quad\times\ \frac{1}{2}\left[\varepsilon^{-1}_{\mathbf{G}_1,\mathbf{G}_2}(\mathbf{q},\omega=0)-\delta_{\mathbf{G}_1,\mathbf{G}_2}\right]\frac{4\pi\, e^2}{\Omega|\mathbf{q}+\mathbf{G}_2|^2} &(11)\\
&= \frac{1}{2\Omega}\sum_{\mathbf{q},\mathbf{G}_3}\left[\varepsilon^{-1}_{\mathbf{G}+\mathbf{G}_3,\mathbf{G}'+\mathbf{G}_3}(\mathbf{q},\omega=0)-\delta_{\mathbf{G},\mathbf{G}'}\right]\frac{4\pi\, e^2}{\Omega|\mathbf{q}+\mathbf{G}'+\mathbf{G}_3|^2}.
\end{aligned}$$

The last line in Eq. (11) can be derived from the completeness relation of the Bloch wave functions (5). The approximation of a statically screened Coulomb interaction (i.e. $\omega=0$ in Eqs. 10 and 11) makes these self energy contributions much simpler than their dynamically screened counterparts (B3a) and (B3b) in Ref.[23]. More importantly, the self energy is now essentially determined and controlled by the inverse dielectric matrix $\varepsilon^{-1}_{\mathbf{G},\mathbf{G}'}(\mathbf{q},\omega=0)$ which accounts correctly for inhomogeneous but static screening[41,42]. The static COHSEX formalism has been further approximated by Baroni et al.[22] who studied LiH with the dielectric function of a homogeneous electron gas, i.e., a diagonal dielectric matrix $\varepsilon^{-1}_{\mathbf{G},\mathbf{G}'}(\mathbf{q},\omega=0)=\varepsilon^{-1}_{\mathrm{hom}}[|\mathbf{q}+\mathbf{G}|,\omega=0]\,\delta_{\mathbf{G},\mathbf{G}'}$. With such a dielectric matrix Eq. (11) reduces to a much simpler integral [Eq. (5) of Ref.[22]]. The Coulomb hole around an electron in such a theory is independent of the quasi-particle state the electron occupies resulting in a constant energy shift of all bands[22] and corresponding to $\Sigma^{\mathrm{COH}}_{\mathbf{G},\mathbf{G}'}=E_{\mathrm{CH}}\,\delta_{\mathbf{G},\mathbf{G}'}$. A Hartree Fock calculation[43] goes even further and corresponds to $\varepsilon^{-1}_{\mathbf{G},\mathbf{G}'}(\mathbf{q},\omega=0)=\delta_{\mathbf{G},\mathbf{G}'}$. The latter case is a mean field theory which neglects any spatial correlations in the electronic system. The Coulomb hole self energy contribution vanishes in the Hartree Fock approximation, i.e., $\Sigma^{\mathrm{COH}}_{\mathbf{G},\mathbf{G}'}=0$. In the following we will see that *inhomogeneous* screening[41,42], i.e.

off diagonal elements in the dielectric matrix $\varepsilon^{-1}_{\mathbf{G},\mathbf{G}'}(\mathbf{q},\omega=0)$, has a crucial influence on both the stationary $\rho_0(\mathbf{r})$ and transient $\rho(\mathbf{r},t)$ electron distributions of LiH exposed to strong electric fields, a phenomenon which could not be observed in the theory of Baroni et al.[22], since such phenomena are excluded from the very beginning.

In order to be as close as possible to experimentally measured physical quantities of LiH we did not use *ab initio* static dielectric matrices [cf. section III.A of Ref.[23]] but (similar to section II.C of Ref.[22]) constructed a model dielectric matrix $\varepsilon^{-1}_{\mathbf{G},\mathbf{G}'}(\mathbf{q},\omega=0)$ which coincides with various measured experimental values of LiH. The basic idea of our approach is that in the sub-volume around each type of atom we introduce an individual *homogeneous* dielectric function of the Baroni type [Eqs. (8) and (9) of Ref.[22]]

$$\begin{aligned}
\varepsilon^{-1}_{\mathrm{Li}}(q,\omega=0) &= \frac{1}{\varepsilon_S}+c_{1,\mathrm{Li}}\frac{q^2}{q^2+k^2_{1,\mathrm{Li}}}+c_{2,\mathrm{Li}}\frac{q^2}{q^2+k^2_{2,\mathrm{Li}}} &(12)\\
\varepsilon^{-1}_{\mathrm{Li}}(q\to\infty,\omega=0) &= 1-\frac{16\pi\, n_{e,\mathrm{Li}}}{a_B}\frac{1}{q^4}+O\left[\frac{1}{q^6}\right]+\cdots &(13)\\
\varepsilon^{-1}_{\mathrm{H}}(q,\omega=0) &= \frac{1}{\varepsilon_S}+c_{1,\mathrm{H}}\frac{q^2}{q^2+k^2_{1,\mathrm{H}}}+c_{2,\mathrm{H}}\frac{q^2}{q^2+k^2_{2,\mathrm{H}}} &(14)\\
\varepsilon^{-1}_{\mathrm{H}}(q\to\infty,\omega=0) &= 1-\frac{16\pi\, n_{e,\mathrm{H}}}{a_B}\frac{1}{q^4}+O\left[\frac{1}{q^6}\right]+\cdots &(15)
\end{aligned}$$

From the experiment we take the static dielectric constant $\varepsilon_S=3.61$ of LiH and the average electron densities around the Li-atom $n_{e,\mathrm{Li}}$ and the H-atom $n_{e,\mathrm{H}}$. As discussed in Ref.[22], the term of type q^{-2} must be rigorously lacking in the aymptotic behavior $q\to\infty$. Its presence would give rise to unphysical divergences in the response to a point-charge perturbation[44]. The constraints determined by the asymptotic behaviors (13) and (15) leave the screening vector $k_{1,\mathrm{Li}}$ (Eq. (12)) and the screening vector $k_{1,\mathrm{H}}$ (Eq. (14)) as free (fitting) parameters in our calculation. The construction of the model dielectric matrix is now straightforward. We assume that the screening of the Coulomb potential between two point charges at positions $\mathbf{r}$ and are $\mathbf{r}'$ within the LiH crystal is determined by the sub-volume of the unit cell in which the center of gravity $\mathbf{R}=(\mathbf{r}+\mathbf{r}')/2$ falls. Putting the Li nucleus into the origin of the unit cell leads to the following dielectric matrix for LiH

$$\begin{aligned}
\varepsilon^{-1}_{\mathbf{G},\mathbf{G}'}(\mathbf{q},\omega=0) &= \frac{\Omega_{\mathrm{Li}}}{\Omega_{\mathrm{uc}}}\exp\left(-\beta^2|\mathbf{G}-\mathbf{G}'|^2\right)\varepsilon^{-1}_{\mathrm{Li}}\left(\left|\mathbf{q}+\frac{\mathbf{G}+\mathbf{G}'}{2}\right|,\omega=0\right)\\
&\quad+\left[\delta_{\mathbf{G},\mathbf{G}'}-\frac{\Omega_{\mathrm{Li}}}{\Omega_{\mathrm{uc}}}\exp\left(-\beta^2|\mathbf{G}-\mathbf{G}'|^2\right)\right]\\
&\qquad\times\varepsilon^{-1}_{\mathrm{H}}\left(\left|\mathbf{q}+\frac{\mathbf{G}+\mathbf{G}'}{2}\right|,\omega=0\right). \qquad (16)
\end{aligned}$$

The length β in (16) determines the size of the bell-shaped screening volume Ω_{Li} around the Li-atom and in turn the partitioning of the average electron

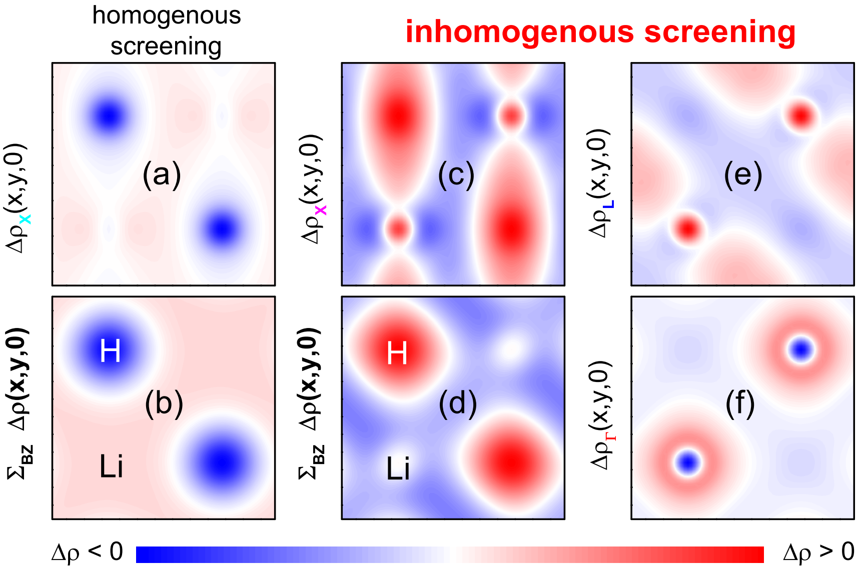

Fig. 9 (a) and (c) Deformed electron densities at the X point, (e) L-point, and (f) Γ-point within the BZ for an external field amplitude of $|\mathbf{E}| = 10^9$ V/m. (b) and (d) Summation over the Brillouin zone gives the total density change $\Delta\rho_{\mathrm{Sym}}(x,y,0,t=0)$ calculated with Eq. (3). The respective charge integrations over $(a/2)^3$-boxes yield (b) $\Delta q_H = -0.1\ e^-$ and (d) $\Delta q_H = +0.01\ e^-$. Panels (a) and (b) correspond to calculation with homogeneous screening similar to that of Ref.[22]. Panels (c,d,e,f) are calculated with a somewhat stronger screening on the proton resulting in 2P-like orbitals on both Li and H nuclei at the X-point (zone boundary).

densities $n_{e,\mathrm{Li}}\ \Omega_{\mathrm{Li}} + n_{e,\mathrm{H}}\ [\Omega_{\mathrm{uc}} - \Omega_{\mathrm{Li}}] = 4$ in Eqs. (13) and (15). For different $\varepsilon_{\mathrm{Li}}^{-1}(q,\omega=0) \neq \varepsilon_{\mathrm{H}}^{-1}(q,\omega=0)$ the dielectric matrix (16) gets off-diagonal elements which account for the *inhomogeneous* screening in LiH. Choosing a common dielectric function $\varepsilon_{\mathrm{Li}}^{-1}(q,\omega=0) = \varepsilon_{\mathrm{H}}^{-1}(q,\omega=0) = \varepsilon_{\mathrm{hom}}^{-1}(q,\omega=0)$ we can recover the *homogeneous* screening result of Baroni et al.[22].

In solving Eq. (6), we expanded the quasi-particle band structure in plane waves using 339 reciprocal lattice vectors in a sphere around the Γ-point with radius $\mathbf{G}_{hkl} < 7 \times 2\pi/a$. For the $\mathbf{k}$ summations in Eqs. (8), (10), and (11) we used the 10 special points (and their symmetry equivalents) in the Brillouin zone of Ref.[45]. In order to delete the singularity of the Coulomb potential in Eqs. (10) and (11) we used the method described with Eq. (3.13) by Ohkoshi[43].

As a start we repeated both the Hartree Fock (Fig. 1 of Ref.[22]) and the COHSEX calculation with *homogeneous* screening (Fig. 5 of Ref.[22]) of Baroni et al. and found a very good agreement of the band structures with our calculations [cf. Fig. 8(a)]. A significant discrepancy between experiment and theory is observed, however, when looking at the electron density map $\rho_0(\mathbf{r})$. In both the Hartree Fock and the COHSEX calculation with *homogeneous* screening, the valence band is dominated by 1S-like orbitals on the H atom throughout the Brillouin zone[26]. As a consequence, the calculated stationary electron density correspond to the fully ionized $\mathrm{Li}^+\ \mathrm{H}^-$ situation. This is in strong contrast to the stationary x-ray diffraction experiments[29,30]. Counting the charges in LiH gives $\mathrm{Li}^{0.5+}\mathrm{H}^{0.5-}$, striking a happy medium between the ionic case $\mathrm{Li}^{+}\mathrm{H}^{-}$ and the so-called covalent case $\mathrm{Li}^{0+}\mathrm{H}^{0-}$ in which electrons are shared between lithium and hydrogen. Obviously, a quasi-particle theory with *homogeneous* screening[22] misses key features of the electron correlations in LiH.

The COHSEX model discussed above allows for studying the influence of *inhomogeneous* screening on the electron correlations in LiH. To this end, we varied the screening vectors $k_{1,\mathrm{Li}}$ and $k_{1,\mathrm{H}}$ and the length β characterizing the size of the screening volume around Li in order to simultaneously fit the quasi-particle band structure [experimental values from Table V in Ref.[22]] and the stationary electron density [x-ray diffraction experiment from Ref.[30]]. The length β was chosen that the gaussian-shaped screening volume around the Li nucleus has the same width as the electron density on the Li-atom. It turned out that small variations of β around this starting value do not have a strong influence on both the band structure and the electron density $\rho_0(\mathbf{r})$.

Our calculations show that modifying the screening vectors $k_{1,\mathrm{Li}}$ and $k_{1,\mathrm{H}}$ in the COHSEX calculation of LiH allows for a gradual transition from $3\mathrm{e}^-$ on Li^{3+} (metal-like wave functions) to $2\mathrm{e}^-$ on Li^{3+} (insulator-like wave functions). Thus, the experimental value of $2.5\mathrm{e}^-$ on Li^{3+} shows that LiH is at the very limit of an metal-insulator transition[24,25]. We found a good agreement with the quasi-particle band structure [experimental values from table V. in Ref.[22]] and the stationary electron density [x-ray diffraction experiment from Ref.[30]] when choosing $k_{1,\mathrm{H}}/k_{1,\mathrm{Li}} = 2$ and $k_{1,\mathrm{H}} \times k_{1,\mathrm{Li}} = k_{1,\mathrm{hom}}^2$ with $k_{1,\mathrm{hom}}$ being the Thomas Fermi screening vector of the *homogeneous* electron gas as used in Ref.[22]. In simple words, a stronger screening in the volume around the H-atom tries to repel the second electron from being attached to the H-atom. The corresponding band structure with *inhomogeneous* screening is shown in Fig. 8(c).

Next, we introduce light-matter interaction into our COHSEX model by making the so called minimal substitution in the kinetic energy term of the hamiltonian Eq. (7):

$$\frac{\hbar^2|\mathbf{k}+\mathbf{G}|^2}{2m}\delta_{\mathbf{G},\mathbf{G}'} \Longrightarrow \frac{\hbar^2|\mathbf{k}+\mathbf{G}-e\mathbf{A}(t)|^2}{2m}\delta_{\mathbf{G},\mathbf{G}'}. \tag{17}$$

Eq. 17 is valid for a spatially homogeneous but time-dependent electric field $\mathbf{E}(t)$ with the usual relation to the vector potential $\mathbf{A}(t) = \int_{-\infty}^{t} dt'\, \mathbf{E}(t')$. Since in the COHSEX approach applied here the self energy operator in (6) does not depend on the quasi-particle energy itself we can also substitute on the r.h.s. of (6) the eigenvalue $E_{n,\mathbf{k}}\psi_{n,\mathbf{k}}(\mathbf{G}) \Longrightarrow i\hbar\partial\psi_{n,\mathbf{k}}(\mathbf{G})/\partial t$ to gain a nonlinear "Schrödinger equation" for the quasi-particles. In such a time-dependent COHSEX calculation all quantities including the self-energy became also time-dependent and had to be updated for each individual time step on the order of a few attoseconds. An advantage of time-dependent COHSEX is that it can also be used in the regime of non-perturbative light-matter interaction to investigate nonlinear electron correlations. On the other hand, such a theory is almost numerically intractable. Here, we study our system in linear response to an external electric field $\mathbf{E}(t)$ oscillating at a frequency much lower than the lowest interband transition frequency. As a result, exclusively bound electrons interact with the external field. Such conditions are well matched with Eq. 1.10 of Ref.[16] from which we learn that the time-independent ground state electron correlations (i.e. the time-independent ground state self energy) determine the linear response to $\mathbf{E}(t)$. As a consequence we can use time-independent perturbation theory as done with Eq. (2) discussed above. Within our COHSEX formalism the optical interband dipole moments are calculated with help of[14]

$$\langle \Psi_{b',\mathbf{k}} | e\mathbf{r} | \Psi_{b,\mathbf{k}} \rangle = \frac{i\, e\, \hbar^2}{m} \sum_{\mathbf{G}} \frac{\psi^*_{b',\mathbf{k}}(\mathbf{G})\, [\mathbf{k}+\mathbf{G}]\, \psi_{b,\mathbf{k}}(\mathbf{G})}{E_{b,\mathbf{k}} - E_{b',\mathbf{k}}}. \tag{18}$$

With this theoretical framework, we now investigate the deformation of the electron density in LiH in a strong electric field for two dielectric matrices: (i) using *homogeneous* screening with parameters of Baroni et al.[22] and (ii) using *inhomogeneous screening* with the parameters of our best fit for band structure [experimental values from table V. in Ref.[22]] and stationary electron density [x-ray diffraction experiment from Ref.[30]]. The calculations using eqs. (2) and (3) are summarized in Figs. 8 and 9. In the left panels of the two figures, we show 8(a) the bandstructure, 8(b) the valence band electron density ρ_X at the X point where the smallest bandgap occurs, 9(a) the field-induced change of electron density at the X point, and 9(b) the total change of electron density calculated with Eq. (3). This calculation assumes a homogeneous screening with the parameters of Ref.[22]. As in mean field calculations, i.e., Hartree Fock, the valence band is dominated by 1S-like orbitals on the H atom throughout the Brilluoin zone[26]. As a consequence, the stationary electron density correspond to the fully ionized Li^+ H^- situation. Applying an electric field would reduce the charge on the H^- anion by $\Delta q_H = -0.1\, e^-$ [Fig. 9(b)], a behavior in striking contrast to our experimental results for LiH [Fig. 6(c,f)] but close to the behavior of NaBH_4 [Fig. 6(a,d)]. In contrast, panels (c-f) of Figs. 8 and 9 are calculated using the COHSEX model with *inhomogeneous screening* and parameters of our best fit for the stationary electron density. In contrast to the homogeneous screening case the valence band Bloch functions depend now sensitively on their wave vector within the Brillouin zone (BZ). At the Γ-point [Fig. 9(f)] the valence band Bloch function has a strong contribution of 2S-like orbitals on the Li-atoms, whereas at the L-point (e) complex hybrid-orbitals on both the H- and Li-atom are formed. Most importantly, the Bloch functions develop into 2P-like orbitals on both Li and H nuclei when approaching the valence band at the X-point [Fig. 8(d)]. Under the external electric field, we observe a general trend of the deformed electron density at any point (wave vector) within the BZ. The electric field distributes the electronic charge more uniformly within the unit cell, causing in turn a reduction of amplitude of the highest peaks as observed for $\Delta\rho_X(x,y,0)$, $\Delta\rho_L(x,y,0)$, and $\Delta\rho_\Gamma(x,y,0)$ in panels (c,e,f) of Fig. 9. As a consequence, we have simultaneously both a transfer of electronic charge from H to Li and from Li to H, sensitively depending of the wave vector of the Bloch function. The electronic correlations in LiH determine which direction of electron transfer will dominate in the summation over the entire BZ. The COHSEX calculation with *inhomogeneous* screening shows that the electron density of H^+ increases at the X point and its vicinity which dominates the total charge increase on the H-atom by $\Delta q_H = +0.01\, e^-$ [Figs. 9(c) and (d)]. This behavior is in *quantitative* agreement with the femtosecond diffraction experiment on LiH and reveals the strong impact of an *inhomogeneous* enhancement of screening at the H^+ site on the wave functions at the X point.

To summarize, our theoretical study of the impact of *inhomogeneous* screening on the quasi-particle properties in LiH shows that both the Hartree Fock calculation and the COHSEX approximation with homogeneous screening[22] wrongly predict a decrease of ionicity of LiH in a strong electric field. Thus, Coulomb correlations among the electrons in the *inhomogeneous* electron gas of a LiH crystal are essential for a field-driven increase of ionicity of LiH as observed in the femtosecond diffraction experiments.

6 Conclusion

In conclusion, we studied in crystalline $NaBH_4$, $LiBH_4$, and LiH spatially resolved electron density maps determined by femtosecond x-ray powder diffraction in the response to a non-resonant strong electric field. Our experiments reveal the prominent role of electron correlations for the field-induced deformation of the electron density maps. In LiH, field-induced correlations between states in the valence and different conduction bands result in an enhancement of ionicity which is manifested in an electron transfer from Li to H and in agreement with quasi-particle calculations within the COHSEX formalism. In contrast, both $NaBH_4$ and $LiBH_4$ display an electron transfer from BH_4^- to the respective cation, as expected for an admixture of states in the lowest conduction band. Furthermore, the distorted geometry of the BH_4 tetrahedron in $LiBH_4$ leads to different contributions of the H atoms to electron transfer. Our results demonstrate the strong potential of femtosecond diffraction methods to uncover microscopic charge dynamics and determine electron transport mechanisms in crystalline matter.

Acknowledgements

This research has received funding from the European Research Council under the European Union's Seventh Framework Programme (FP7/2007-2012)/ERC Grant Agreement 247051 and from the Deutsche Forschungsgemeinschaft (Grant WO 558/13-1).

References

1 W. Kuehn, P. Gaal, K. Reimann, M. Woerner, T. Elsaesser, R. Hey, *Phys. Rev. Lett.*, 2010, **104**, 146602.

2 G. Herink, D. R. Solli, M. Gulde, C. Ropers, *Nature*, 2012, **483**, 190.

3 W. Kuehn, P. Gaal, K. Reimann, M. Woerner, T. Elsaesser, R. Hey, *Phys. Rev. B*, 2010, **82**, 075204.

4 T. E. Glover, D. M. Fritz, M. Cammarata, T. K. Allison, Sinisa Coh, J. M. Feldkamp, H. Lemke, D. Zhu, Y. Feng, R. N. Coffee, M. Fuchs, S. Ghimire, J. Chen, S. Shwartz, D. A. Reis, S. E. Harris, J. B. Hastings, *Nature*, 2012, **488**, 603.

5 M. Schultze, E. M. Bothschafter, A. Sommer, S. Holzner, W. Schweinberger, M. Fiess, M. Hofstetter, R. Kienberger, V. Apalkov, V. S. Yakovlev, M. I. Stockman, F. Krausz, *Nature*, 2013, **493**, 75.

6 A. Schiffrin, T. Paasch-Colberg, N. Karpowicz, V. Apalkov, D. Gerster, S. Mhlbrandt, M. Korbman, J. Reichert, M. Schultze, S. Holzner, J. V. Barth, R. Kienberger, R. Ernstorfer, V. S. Yakovlev, M. I. Stockman, F. Krausz, *Nature*, 2013, **493**, 70.

7 T. Elsaesser, M. Woerner, *J. Chem. Phys.*, 2014, **140**, 020901.

8 M. Bargheer, N. Zhavoronkov, Y. Gritsai, J.C. Woo, D.S. Kim, M. Woerner, T. Elsaesser, *Science*, 2004, **306**, 1771.

9 M. Woerner, F. Zamponi, Z. Ansari, J. Dreyer, B. Freyer, M. Prémont-Schwarz and T. Elsaesser, *J. Chem. Phys.*, 2010, **133**, 064509.

10 F. Zamponi, P. Rothhardt, J. Stingl, M. Woerner, and T. Elsaesser, *Proc. Nat. Acad. Sci. USA*, 2012, **109**, 5207.

11 B. Freyer, F. Zamponi, V. Juv, J. Stingl, M. Woerner, T. Elsaesser, M. Chergui, *J. Chem. Phys.*, 2013, **138**, 144504.

12 J. Stingl, F. Zamponi, B. Freyer, M. Woerner, T. Elsaesser, and A. Borgschulte, *Phys. Rev. Lett.*, 2012, **109**, 147402.

13 V. Juvé, M. Holtz, F. Zamponi, M. Woerner, T. Elsaesser, A. Borgschulte, *Phys. Rev. Lett.*, 2013, **111**, 217401.

14 C. Cohen-Tannoudji, B. Diu and F.Laloë, *Quantum Mechanics*, Vol. 1-2 , Wiley Interscience Publication, New York, 1977.

15 D. H. Ewing, F. Seitz, *Phys. Rev.*, 1936, **50**, 760.

16 W. Kohn, *Phys. Rev.*, 1957, **105**, 509.

17 R. E. Behringer, *Phys. Rev.*, 1959, **113**, 787.

18 G. W. Pratt, Jr., *Phys. Rev.*, 1960, **118**, 462.

19 P. Hohenberg, W. Kohn, *Phys. Rev.*, 1964, **136**, B864.

20 L. Hedin, *Phys. Rev.*, 1965, **139**, A796.

21 K.-F. Bergren, *J. Phys. C (solid st. phys.)*, 1969, **2**, 802.

22 S. Baroni, G. Pastori Parravicini, G. Pezzica, *Phys. Rev. B*, 1985, **32**, 4077.

23 M. S. Hybertsen, S. G. Louie, *Phys. Rev. B*, 1986, **34**, 5390.

24 L. Bellaiche, J. M. Besson, K. Kunc, B. Lévy, *Phys. Rev. Lett.*, 1998, **80**, 5576.

25 S. Lebégue, M. Alouani, B. Arnaud, W. E. Pickett, *Europhys. Lett.*, 2003 **63**, 562.

26 N. Novakovic, I. Radisavljevic, D. Colognesi, S. Ostojic, N. Ivanovic, *J. Phys.: Cond. Mat.*, 2007, **19**, 406211.

27 F. Zamponi, Z. Ansari, M. Woerner, and T. Elsaesser, *Opt. Express*, 2010, **18**, 947.

28 N. Zhavoronkov, Y. Gritsai, M. Bargheer, M. Woerner, Th. Elsaesser, F. Zamponi, I. Uschmann, and E. Förster, *Opt. Lett.*, 2005 **30**, 1737.

29 R. S. Calder, W. Cochran, D. Griffiths, R. D. Lowde, *J. Phys. Chem. Sol.*, 1962 **23**, 621.

30 G. Vidal-Valat, J.-P. Vidal, *Acta Cryst. A*, 1992, **48**, 46.

31 P, Fischer, A. Züttel, *Mat. Sci. Forum*, 2004, Vols. **443-444**, 287.

32 R. S. Kumar, A. L. Cornelius, *Appl. Phys. Lett.*, 2005, **87**, 261916.

33 J. Soulié, G. Renaudin, R. Cerny and K. Yvon, *Journal of alloys and compounds*, 2002, **346**, 200.

34 E. Jaynes, *Phys. Rev.*, 1957, **108**, 171.

35 C. Gilmore, *Acta Cryst. A*, 1996 **52**, 561.

36 M. Sakata and M. Sato, *Acta Crystallogr. Sec. A*, 1990, **46**, 263.

37 S. Smaalen, L. Palatinus, and M. Schneider, *Acta Cryst. A*, 2003, **59**, 459.

38 P. Coppens, *X-Ray Charge Densities and Chemical Bonding*, Oxford University Press, 1997.

39 D.M. Collins, *Nature*, 1982, **298**, 49.

40 L. Palatinus. *Maximum Entropy Method in Superspace Crystallography*, PhD thesis, University of Bayreuth, Germany, 2003.

41 N. Wiser, *Phys. Rev.*, 1963, **129**, 62.

42 A. Baldereschi, E. Tosatti, *Sol. Stat. Commun.*, 1979, **29**, 131.

43 I. Ohkoshi, *J. Phys. C:Solid State Phys.*, 1985, **18**, 5415.

44 J. S. Langer and S. H. Vosko, *J. Phys. Chem. Solids*, 1959, **12**, 196.

45 D. J. Chadi and M. L Cohen, *Phys. Rev. B*, 1973, **8**, 5747.